CHIN. PHYS. LETT. Vol. 38, No. 7 (2021) 077101

Dual Topological Features of Weyl Semimetallic Phases in Tetradymite $BiSbTe_3$

Z. Z. Zhou(周宇桢)[1], H. J. Liu(刘惠军)[2], G. Y. Wang(王国玉)[3], R. Wang(王锐)[1*], and X. Y. Zhou(周小元)[1*]

[1]*Center for Quantum Materials and Devices, College of Physics, Chongqing University, Chongqing 401331, China*
[2]*Key Laboratory of Artificial Micro- and Nano-Structures of Ministry of Education, and School of Physics and Technology, Wuhan University, Wuhan 430072, China*
[3]*Chongqing Institute of Green and Intelligent Technology, Chinese Academy of Science, Chongqing 400714, China*

(Received 11 March 2021; accepted 30 April 2021; published online 3 July 2021)

Based on first-principles calculations and symmetry arguments, we reveal that the non-centrosymmetric ternary tetradymite $BiSbTe_3$ possesses exotic dual topological features of Weyl semimetallic phases with Z_2 index (1:000). The results show that the helical Dirac-type surface states protected by the time-reversal symmetry are present in the vicinity of the Brillouin zone center, which is consistent with the experimental report. Furthermore, we show that four pairs of Weyl points reside exactly at the Fermi level, which are guaranteed to be located on high-symmetry planes due to mirror symmetries. The helical surface states and the projected Weyl nodes are well separated in the momentum space, facilitating their observations in experiments. This work not only uncovers a unique quantum phenomenon with dual topological features in the tetradymite family but also paves a fascinating avenue for exploring the coexistence of multi-topological states with wide applications.

DOI: 10.1088/0256-307X/38/7/077101

Materials with a nontrivial band topology have guided significant advances over the past decade due to the fundamental scientific importance and immense potential applications.[1−3] A representative example is the surface states of topological insulators (TI), in which the suppressed backscattering channels favor dissipationless electronic conduction.[4,5] Subsequently, a new class of topological quantum materials named Weyl semimetals (WSMs) have been discovered,[6−9] in which the band crossed points (i.e., Weyl points) with linear dispersions near the Fermi level, and can be characterized by the Weyl equation.[10] The Weyl points with opposite chirality always appear in pairs,[10] which are separated in momentum space via breaking either the inversion ($\mathcal{I}$) or time-reversal ($\mathcal{T}$) symmetry. Intriguingly, the exotic bulk and surface states in WSMs have induced various manifestations such as negative magnetoresistance[11] and chiral anomaly,[12] which also stimulated extensive investigations for the functionalities including valley polarization[13] and magnetization switching.[14]

Since the binary Bi_2Te_3, Bi_2Se_3, and Sb_2Te_3 were demonstrated to be strong TIs both theoretically and experimentally,[15,16] tetradymite compounds have received increasing attention owing to the intimate link between the band topology and realistic applications.[17−19] For instance, topological tetradymites provide ideal platforms for exploring the coupling mechanism between the nontrivial surface states and thermoelectric effects.[20−22] To date, many tetradymites have been identified to be strong TIs, e.g., Sb_2Te_2S, Sb_2Te_2Se, Bi_2Te_2Se, Bi_2Se_2Te, and $BiSbSeTe_2$.[23−25] In particular, Cao *et al.*[26] proposed a two-dimensional descriptor to scan a huge number of TIs in the tetradymite family based on high-throughput prediction. Despite the rapid progress in screening TIs, tetradymites with WSM features have rarely been observed. One important reason is that the band extrema of tetradymite with strong spin-orbital coupling (SOC) do not locate at the high-symmetry lines,[27] making the possible nodal points hidden in the Brillouin zone (BZ). In contrast to conventional materials with the individual topological phase, tetradymite compounds are expected to host multiple topological features at distinct positions in momentum space, which are highly desirable for the study of coexisting topological features. Hence, a previously uncharted and much meaningful material space with unconventional topological quantum phenomena remains largely unexplored in the tetradymite family.

In this Letter, we show that the non-centrosymmetric ternary tetradymite $BiSbTe_3$ satisfies the criteria mentioned above. Using first-principles calculations combined with a $\boldsymbol{k}\cdot\boldsymbol{p}$ model analysis, we demonstrate the presence of exotic dual topological features, which has not been reported in realistic material up to now. Apart from the topological inverted gap near the Γ point, we reveal that there are four pairs of Weyl points located on high-

Supported by the National Natural Science Foundation of China (Grant Nos. 11604032, 11674040, and 51672270), and the Fundamental Research Funds for the Central Universities (Grant No. 106112016CDJZR308808).
*Corresponding authors. Email: rcwang@cqu.edu.cn; xiaoyuan2013@cqu.edu.cn
© 2021 Chinese Physical Society and IOP Publishing Ltd

symmetry planes rather than high-symmetry lines. This study offers a feasible platform for investigating the coexistence of multi-topological phases with unconventional nontrivial surface states.

Methods. Based on density functional theory (DFT), the electronic band structures of $BiSbTe_3$ were calculated with the projector augmented wave approach,[28,29] as implemented in the Vienna *ab initio* simulation package.[30–32] The Perdew–Burke–Ernzerhof (PBE) functional with the generalized gradient approximation[33] was employed in structural relaxation and electronic calculations. A $15 \times 15 \times 15$ Monkhorst–Pack $\boldsymbol{k}$-mesh was adopted for the BZ integrations with the kinetic-energy cutoff set to be 550 eV. The SOC effect and the van der Waals (vdW) interactions with the form of optB86b-vdW[34] were explicitly included in our calculations. In addition, partially self-consistent GW_0 calculations with a $6 \times 6 \times 6\Gamma$ centered $\boldsymbol{k}$-grid were performed to accurately predict the electronic band structures of $BiSbTe_3$. Based on the maximally localized Wannier functions,[35] the topological surface states were studied via the iterative Green's function method,[36] as implemented in the so-called WANNIERTOOLS package.[37] To ensure the reliability, all the calculated results were rechecked by the MBJ method as shown in Fig. S3 of the Supplemental Material.

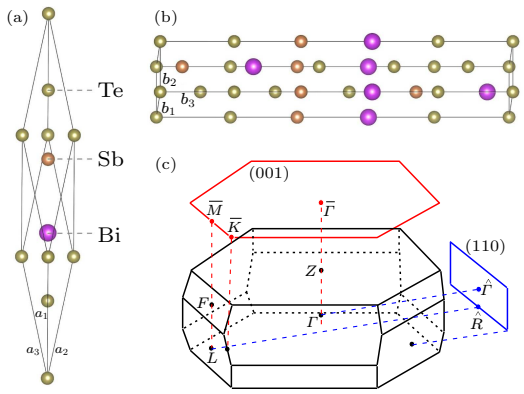

Fig. 1. (a) The primitive cell and (b) conventional cell of $BiSbTe_3$. (c) The BZ of the primitive cell as well as the surface BZs of (001) and (110) planes.

Results and Discussions. Tetradymite with the $\mathcal{I}$ symmetry such as Bi_2Te_3 crystalizes in a rhombohedral structure belonging to the space group $R\bar{3}m$ (No. 166). By substituting one Bi atom with Sb element for each quintuple layer shown in Figs. 1(a) and 1(b), the $\mathcal{I}$ symmetry breaking induces that the space group of the ternary $BiSbTe_3$ transforms to be $R3m$ (No. 160). In this case, the $\mathcal{T}$ symmetry and three reflection symmetries with respect to the (100), (010), and (110) mirror planes are preserved. Figure 1(c) plots the bulk BZ and the surface BZs in (110) and (001) plane. The high-symmetry points are also projected to the corresponding surface. The optimized lattice parameters of $BiSbTe_3$ are calculated to be $a = 4.344$ Å and $c = 30.518$ Å for the conventional cell, which nicely agree with the experimental results.[38] It is noteworthy that the single crystal of $BiSbTe_3$ in a disorder phase has already been synthesized experimentally due to its excellent thermoelectric performance,[39] which ensures the existence of the tetradymite with such a stoichiometry. Additionally, we have calculated the phonon dispersion relations of $BiSbTe_3$ as plotted in Fig. S4 of the Supplemental Material. There is no imaginary frequency, guaranteeing the dynamic stability. The formation energy of $BiSbTe_3$ is also evaluated by Sb-doping in Bi_2Te_3. The calculated formation energy is -28 meV/primitive-cell, which indicates the energetic stability. Moreover, we have calculated the total energy of the noncentrosymmetric $BiSbTe_3$, which is 46 meV/primitive-cell lower than that of the inversion symmetric system. Here we achieve the inversion symmetric $BiSbTe_3$ by constructing a $1 \times 1 \times 2$ supercell with nominal formula of $Bi_2Sb_2Te_6$. Therefore, it is convincing that the noncentrosymmetric $BiSbTe_3$ is stable, implying that $BiSbTe_3$ will be verified further in experiments.

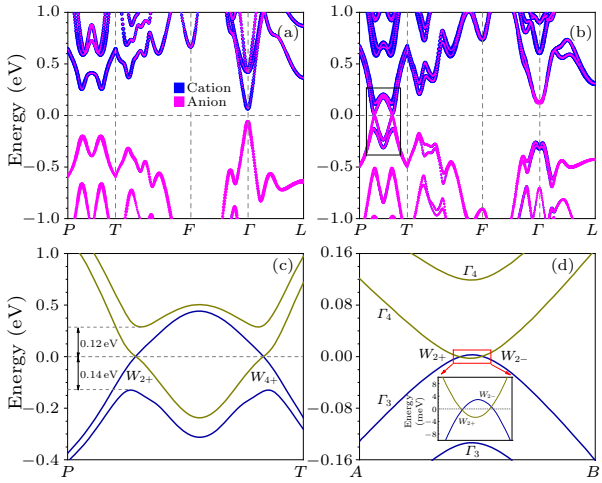

Fig. 2. The orbital-decomposed band structures of $BiSbTe_3$ (a) without and (b) with SOC. The P and T are not the high-symmetry points with the coordinates of (0.402, 0.500, 0.210) and (0.402, 0.210, 0.500), respectively. (c) Enlarged view of the Weyl points framed in (b). (d) The band structures along the direction containing W_{2+} and W_{2-} points. The coordinates of A and B are (0.094, 0.094, 0.000) and (0.594, 0.594, 0.500), respectively.

Figures 2(a) and 2(b) illustrate the orbital-decomposed band structures of $BiSbTe_3$ without and with SOC, respectively, where the vdW interactions and quasiparticle GW_0 approximation are explicitly considered. In the absence of SOC, $BiSbTe_3$ is predicted to be a normal semiconductor with a direct bandgap of 0.13 eV at the Γ point. By taking into account the SOC, we see from Fig. 2(b) that visible

band inversion arises near the Γ point, which yields topologically protected surface states as demonstrated experimentally.[17] Combining the calculated topological Z_2 invariants of $(v_0 : v_1v_2v_3) = (1 : 000)$ (see Fig. S5 in the Supplemental Material), the nontrivial topological nature of $BiSbTe_3$ can be sufficiently testified as also observed in binary tetradymites. Furthermore, it is found that the band structures exhibit remarkable spin splitting except for the time-reversal invariant $\boldsymbol{k}$-points (Γ, L, and F). Such a fact also reveals the broken $\mathcal{I}$ but reserved $\mathcal{T}$ symmetry, which allows the realization of the Weyl semimetallic phase.[40] Indeed, a total of four pairs of type-I Weyl points can be screened by a careful search in the whole BZ. The corresponding $\boldsymbol{k}$-points are listed in Table 1, as well as their chirality determined via the Wilson-loop method.[37] Interestingly, it is found that all the Weyl points almost exactly reside at the Fermi level, which could maximize the transport phenomena caused by chiral anomaly. In Fig. 2(b), we plot the band structures along the $\boldsymbol{k}$-path containing two Weyl points with the same chirality of +1, among which obvious band inversion is taken place. Hence, $BiSbTe_3$ is a unique quantum material possessing both helical Dirac-type surface states and Weyl semimetallic states. Note that all the Weyl points locate at the genetic $\boldsymbol{k}$-points, where large Zeeman-type splitting is induced by the strong SOC of Bi element in the non-centrosymmetric space group $R3m$. Figure 2(c) is the enlarged view of the Weyl points highlighted by the black rectangle in Fig. 2(b), where the top valance band and bottom conduction band at W_{2+} exhibit giant Zeeman-type splitting of 0.14 eV and 0.12 eV, respectively. The total splitting value is larger than the band gap without SOC, which in turns leads to the band cross at the Fermi level. The dispersions around the band touching points are linear in momentum space implying the Weyl semimetallic state. Additionally, the insulator-metal transition originating from spin splitting in a nonmagnetic system is highly appealing for the applications in spintronics.[41]

Table 1. The coordinates in momentum space and the chirality of eight Weyl points.

		Coordinate	Chirality
$k_x = k_y$ plane	W_{1-}	(−0.422, −0.422, −0.328)	−1
	W_{1+}	(−0.402, −0.402, −0.308)	+1
	W_{2-}	(0.422, 0.422, 0.328)	−1
	W_{2+}	(0.402, 0.402, 0.308)	+1
$k_x = k_z$ plane	W_{3-}	(−0.422, −0.328, −0.422)	−1
	W_{3+}	(−0.402, −0.308, −0.402)	+1
	W_{4-}	(0.422, 0.328, 0.422)	−1
	W_{4+}	(0.402, 0.308, 0.402)	+1

To comprehend the band topology inherent to the crystal symmetry, we show in Fig. 2(d) the band structures with $\boldsymbol{k}$-points turned to W_{2+} and W_{2-} presented at $k_x = k_y$ plane, where the coordinates can be denoted as (k_x, k_x, k_z). Besides the $\mathcal{T}$ symmetry, the little group belongs to $\mathcal{M}$ mirror symmetry, which preserves two irreducible representations of Γ_3 and Γ_4 derived from the character table. The crossed bands adjacent to the Fermi level possess the eigenvalues $+i$ for Γ_3 and $-i$ for Γ_4. Based on a two-band $\boldsymbol{k}\cdot\boldsymbol{p}$ model ignoring the kinetic term, the general 2×2 Hamiltonian can be written as

$$H(k_x, k_y, k_z) = \sum_{i=x,y,z} f_i(k_x, k_y, k_z)\sigma_i, \tag{1}$$

where $f_i(k_x, k_y, k_z)$ and σ_i are the real functions and Pauli matrices, respectively. For the $k_x = k_y$ plane, we consider the combination of $\mathcal{T}$ and $\mathcal{M}$. The Hamiltonian is thus constrained by

$$[H(k_x, k_y, k_z), \mathcal{TM}] = 0. \tag{2}$$

Here $\mathcal{M}$ can be expressed as $i\sigma_z$, and the $\mathcal{T}$ operator can be represented as $-i\sigma_y K$ in the presence of SOC, where K is a complex conjugate operator. The product $\mathcal{TM}$ expressed as $i\sigma_x K$ denotes an antiunitary mirror symmetry. Accordingly, Eq. (2) gives

$$\begin{aligned} f_{x,y}(k_x, k_y, k_z) &= f_{x,y}(-k_y, -k_x, -k_z) \\ f_z(k_x, k_y, k_z) &= -f_z(-k_y, -k_x, -k_z). \end{aligned} \tag{3}$$

Under this condition, the Hamiltonian for the crossed bands should be given by

$$H(k_x, k_x, k_z) = f_x(k_x, k_x, k_z)\sigma_x + f_y(k_x, k_x, k_z)\sigma_y, \tag{4}$$

which allows the presence of Weyl points in $k_x = k_y$ plane. These symmetry-protected Weyl points suggest the robust topological Weyl semimetallic state of $BiSbTe_3$. It should be emphasized that the mirror $k_x = k_y$ plane does not invert the components of k-vectors. Thus, the $\mathcal{TM}$ operator in this work is not an axis, and the $\mathcal{M}$ operator does not change the chirality. To have a better understanding, the graphical representation of the distribution of the symmetry protected Weyl points in the Brillouin zone are plotted in Fig. S6 of the Supplemental Material. Furthermore, we also find that the other four Weyl points in $k_x = k_z$ plane should be accidental nodal points, which do not correspond to any symmetry and easily annihilate each other. Thus, there are a total of four pairs of Weyl points residing on the Fermi level in $BiSbTe_3$. Among them, only the two pairs of Weyl points residing on the $k_x = k_y$ plane are protected by mirror symmetry.

The dual topological features of $BiSbTe_3$ can produce unique nontrivial surface states. Figure 3(a) displays the surface state on (001) plane with a topologically protected Dirac cone lying at ∼0.2 eV below the Fermi level, and the corresponding Fermi surface map as well as the spin texture at the energy of −0.1 eV is plotted in Fig. S7 in the Supplemental Material. Such an observation is in good agreement with the

experimental measurement using angle-resolved photoemission spectroscopy[17] and indicates the helical Dirac-type surface states around the Γ point as also found in binary tetradymites. Remarkably, we find that the surface states are terminated by a projection of bulk Weyl cone in $\overline{\Gamma}$–$\overline{M}$ direction. The Fermi surface map in the (001) plane at the energy of 0.015 eV is plotted in Fig. 3(b), where the continuous Fermi arcs form sixfold pockets reflecting the threefold rotational and $\mathcal{T}$ symmetries. More importantly, it is clear that a discontinuous Fermi arc starts from one Weyl point and ends at the other located along $\hat{\Gamma}$–$\hat{R}$ direction on $k_x = k_y$ surface as shown in Fig. 3(c). The left and right nodes signed by the green and purple point are projected from two Weyl points of W_{2+} and W_{2-}, respectively. It should be mentioned that the positions of each pair of two Weyl points are close to each other, leading to the nearly overlapped projections in $k_x = k_y$ surface. As a result, two Fermi arcs are observed at W_{2+} and W_{2-} points.[42] Additionally, we see from Fig. S8 of the Supplemental Material that the gapless points connected with Fermi arcs are projected from two Weyl nodes of W_{2+} and W_{4+}. Figure 3(d) illustrates the Fermi arcs in the $k_x = k_y$ surface, where a closed loop is clearly visible. It is noted that the surface states corresponding to these two topological features are distinct and well separated in the BZ, which facilitates its experimental measurement.

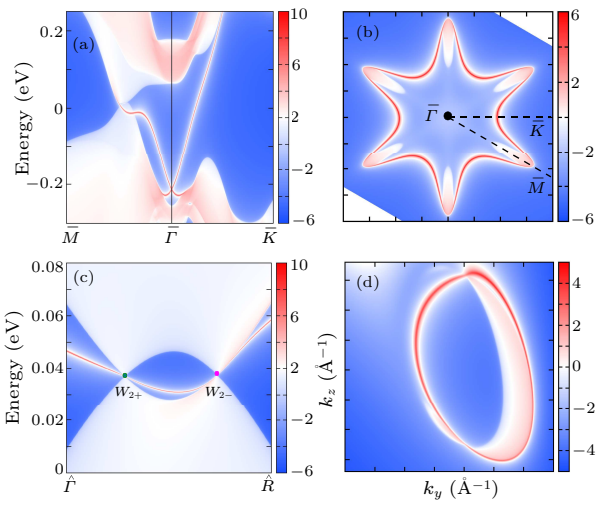

Fig. 3. (a) Surface states projected on the (001) plane and the (b) corresponding Fermi surface. (c) The projected surface states for the $k_x = k_y$ plane along $\hat{\Gamma}$–$\hat{R}$ direction. (d) The Fermi arcs projected on $k_x = k_y$ surface.

It should be mentioned that the nontrivial band topology of some TIs and WSMs are sensitive to the strains.[43–45] Herein, we consider both the compressive and tensile strains along the a- and c-directions, which may have a qualitatively different influence on the topological states.[44] Figures 4(a) and 4(b) plot the band structures of $BiSbTe_3$ in proximity of valance and conduction band edges under in-plane strains with $a = 0.98a_0$ and $a = 1.02a_0$, respectively. In both cases, the symmetry protected Weyl points in the $k_x = k_y$ plane are still reserved with the chirality implied by the evolution of Wannier charge centers, whereas the band crossed points are slightly lifted above the Fermi level. Similar to the cases of the in-plane strain, the Weyl points also reserved for the out-of-plane strains with $c = 0.98c_0$ and $c = 1.02c_0$ as shown in Figs. 4(c) and 4(d), respectively. These Weyl points (see Table S1) are away from the original positions but they are also distributed on $k_x = k_y$ plane, since all symmetries remain under the in-plane or out-of-plane strains. Moreover, our additional calculations manifest that the nonzero topological invariant is not affected by either the in-plane or out-of-plane strains (see Fig. S9 in the Supplemental Material), and the band inversions at the Γ point are always in existence. Such a fact reveals that the topological Z_2 phase protected by the $\mathcal{T}$ symmetry is robust to the perturbations generated by strains. Consequently, the dual nontrivial topological states in $BiSbTe_3$ are impervious to both the in-plane strains and out-of-plane strains.

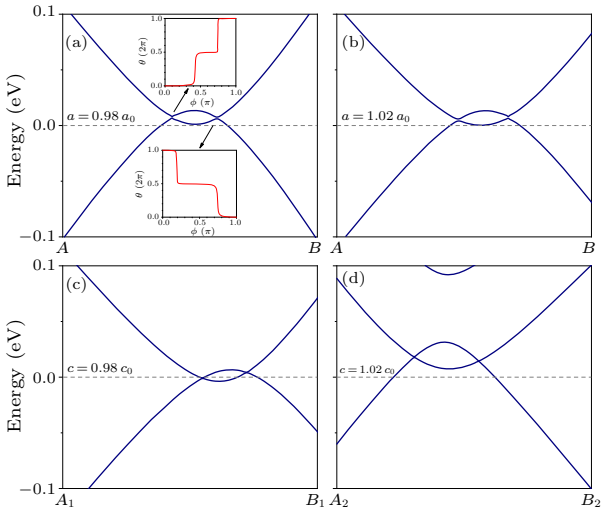

Fig. 4. The band structures of $BiSbTe_3$ under 2% in-plane (a) compressive and (b) tensile strains. The insets show the evolution of the Wannier charge centers around the band crossed points. [(c), (d)] The band structures with 2% compressive and tensile strains along interlayer directions, respectively. The coordinates of A_1, B_1, A_2, and B_2 are (0.100, 0.100, 0.000), (0.600, 0.600, 0.500), (0.091, 0.091, 0.000), and (0.591, 0.591, 0.500), respectively.

In summary, our theoretical study reveals that the ternary tetradymite $BiSbTe_3$ possesses both helical Dirac-type surface states protected by the $\mathcal{T}$ symmetry and ideal Weyl semimetallic features. The discovery of Weyl points lying away from the high-symmetry lines is also reminiscent of the potential WSM concealed in tetradymites without the $\mathcal{I}$ symmetry, which considerably broadens the avenue for fundamental investigation of multiple topological phases. Intrigu-

ingly, the present work proposes a perfect platform to study the interplay between emergent topological nontrivial states and possible applications, especially for the thermoelectricity of tetradymites.

References

[1] Chen H *et al.* 2011 *Phys. Rev. Lett.* **107** 056804
[2] Brüne C *et al.* 2012 *Nat. Phys.* **8** 485
[3] Pei C Y *et al.* 2020 *Chin. Phys. Lett.* **37** 066401
[4] Hasan M Z and Kane C L 2010 *Rev. Mod. Phys.* **82** 3045
[5] Qi X L and Zhang S C 2011 *Rev. Mod. Phys.* **83** 1057
[6] Wan X G *et al.* 2011 *Phys. Rev. B* **83** 205101
[7] Weng H M *et al.* 2015 *Phys. Rev. X* **5** 011029
[8] Soluyanov A A *et al.* 2015 *Nature* **527** 495
[9] Xia B W *et al.* 2019 *Phys. Rev. Lett.* **122** 057205
[10] Nielsen H B and Ninomiya M 1983 *Phys. Rev. Lett.* **130** 389
[11] Son D T and Spivak B Z 2013 *Phys. Rev. B* **88** 104412
[12] Xiong J *et al.* 2015 *Science* **350** 413
[13] Jiang Q D *et al.* 2015 *Phys. Rev. Lett.* **115** 156602
[14] Kurebayashi D and Nomura K 2016 *Phys. Rev. Appl.* **6** 044013
[15] Zhang H *et al.* 2009 *Nat. Phys.* **5** 438
[16] Chen Y L *et al.* 2009 *Science* **325** 178
[17] Zhang J S *et al.* 2011 *Nat. Commun.* **2** 574
[18] Shi H L *et al.* 2015 *Phys. Rev. Appl.* **3** 014004
[19] Yang F *et al.* 2016 *Phys. Rev. B* **94** 075304
[20] Ghaemi P, Mong R S K and Moore J E 2010 *Phys. Rev. Lett.* **105** 166603
[21] Xu Y, Gan Z and Zhang S C 2014 *Phys. Rev. Lett.* **112** 226801
[22] Liang J H *et al.* 2016 *Nanoscale* **8** 8855
[23] Kong D *et al.* 2011 *Nat. Nanotechnol.* **6** 705
[24] Hao G L *et al.* 2013 *J. Appl. Phys.* **113** 024306
[25] Zhou Z Z *et al.* 2018 *J. Phys. D* **51** 315501
[26] Cao G H *et al.* 2020 *Phys. Rev. Mater.* **4** 034204
[27] Cheng L *et al.* 2014 *Phys. Rev. B* **90** 085118
[28] Blöchl P E 1994 *Phys. Rev. B* **50** 17953
[29] Kresse G and Joubert D 1999 *Phys. Rev. B* **59** 1758
[30] Kresse G and Hafner J 1993 *Phys. Rev. B* **47** 558
[31] Kresse G and Hafner J 1994 *Phys. Rev. B* **49** 14251
[32] Kresse G and Furthmüller J 1996 *Comput. Mater. Sci.* **6** 15
[33] Perdew J P, Burke K and Ernzerhof M 1996 *Phys. Rev. Lett.* **77** 3865
[34] Klimeš J, Bowler D R and Michaelides A 2010 *J. Phys.: Condens. Matter* **22** 022201
[35] Mostofi A A *et al.* 2008 *Comput. Phys. Commun.* **178** 685
[36] Sancho M P L, Sancho J M L and Rubio J 1984 *J. Phys. F* **14** 1205
[37] Wu Q S *et al.* 2018 *Comput. Phys. Commun.* **224** 405
[38] Rajput I and Lakhani A 2019 *AIP Conf. Proc.* **2162** 020044
[39] Kulbachinskii V A *et al.* 2012 *AIP Conf. Proc.* **1449** 119
[40] Singh S *et al.* 2016 *Phys. Rev. B* **94** 161116
[41] Acosta C M, Fazzio A and Dalpian G M 2019 *npj Quantum Mater.* **4** 41
[42] Wang R *et al.* 2018 *Phys. Rev. B* **97** 195157
[43] Ruan J W *et al.* 2016 *Nat. Commun.* **7** 11136
[44] Bera A *et al.* 2013 *Phys. Rev. Lett.* **110** 107401
[45] Cao G H *et al.* 2018 *Phys. Rev. B* **97** 075147

Supplementary Material for "Dual Topological Features of Weyl Semimetallic Phases in Tetradymite $BiSbTe_3$"

Z. Z. Zhou(周宇桢)[1], H. J. Liu(刘惠军)[2], G. Y. Wang(王国玉)[3], R. Wang(王锐)[1,*], and X. Y. Zhou(周小元) [1,†]

[1]*Center for Quantum Materials and Devices, College of Physics, Chongqing University, Chongqing 401331, China*

[2]*Key Laboratory of Artificial Micro- and Nano-Structures of Ministry of Education and School of Physics and Technology, Wuhan University, Wuhan 430072, China*

[3]*Chongqing Institute of Green and Intelligent Technology, Chinese Academy of Science, Chongqing 400714, China*

1. The electronic band structures of the $BiSbTe_3$ calculated by DFT and Wannier interpolation technique

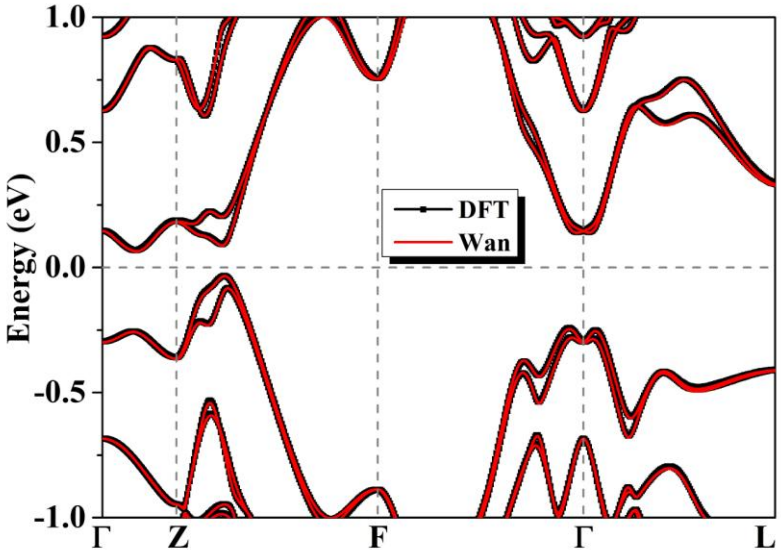

Figure S1. The DFT calculated band structure as compared with that obtained via Wannier interpolation technique. The results agree very well with each other, suggesting the reliability of Wannierization.

[*]Author to whom correspondence should be addressed. Email: rcwang@cqu.edu.cn

[†]Author to whom correspondence should be addressed. Email: xiaoyuan2013@cqu.edu.cn

2. The band structures of the $BiSbTe_3$ calculated by PBE and GW_0

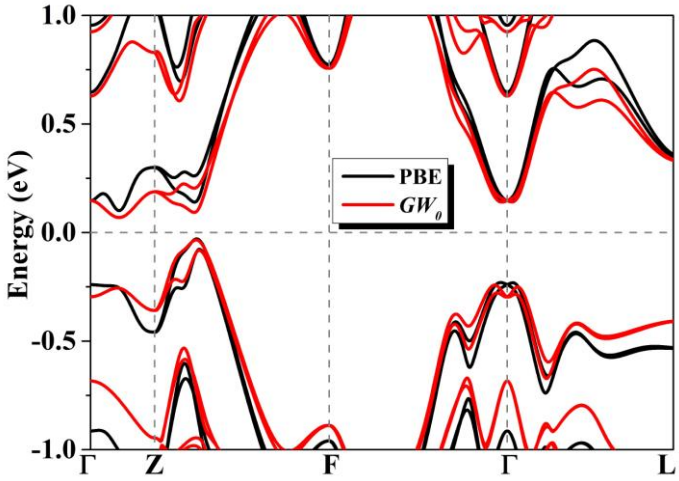

Figure S2. Calculated band structures of $BiSbTe_3$. Black and red lines correspond to the calculations with PBE+optB86b-vdW+SOC and PBE+GW_0+optB86b-vdW+SOC, respectively. The topological features of $BiSbTe_3$ are not affected by considering the GW_0 approximation, whereas the coordinates of band crossed points are slightly different from the PBE calculated results.

3. Recalculated results via MBJ method

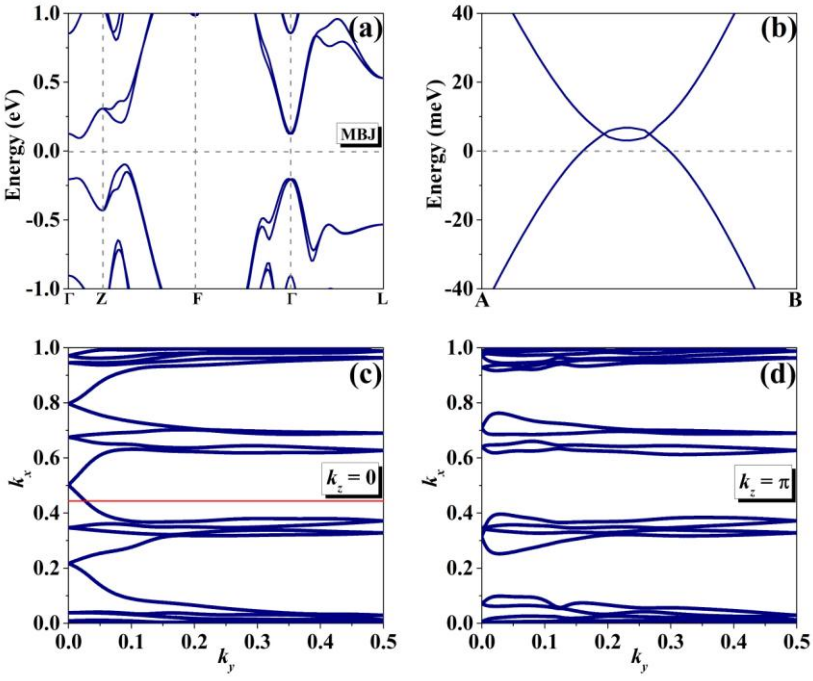

Figure S3. The MBJ calculated band structures along (a) high-symmetry lines and (b) specific line containing two Weyl points. Calculated evolution lines of Wannier centers in (c) $\boldsymbol{k_z} = 0$ and (d) $\boldsymbol{k_z} = \pi$ planes.

We have employed MBJ method to recalculate the band structures and recheck the topological states. The MBJ calculated band structures uncover the same band topology to that calculated from GW_0 method, including the distributions of Weyl points and Z2 topological invariants, as shown Fig. R1. Therefore, all these results confirm the reliability of our calculated results.

4. The phonon dispersion relations of $BiSbTe_3$

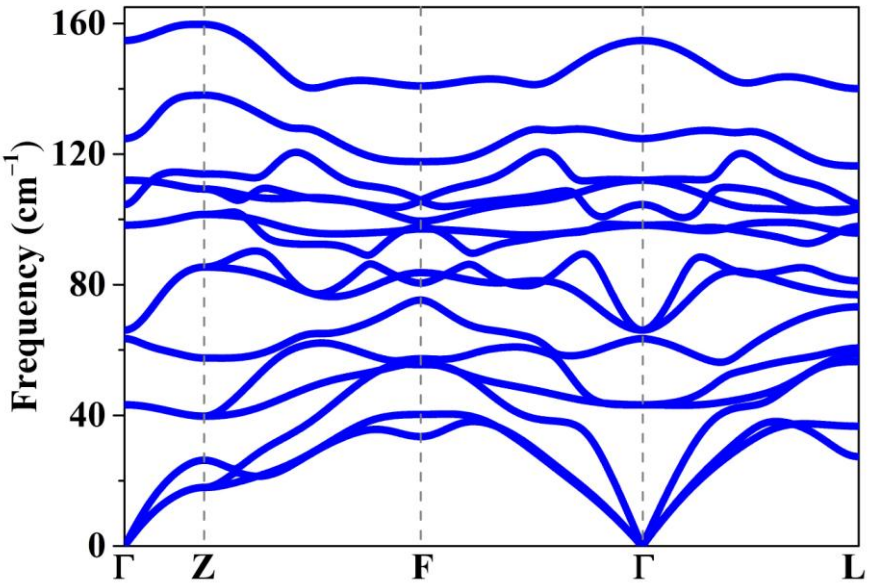

Figure S4. Calculated phonon dispersion relations of $BiSbTe_3$ based on the density functional perturbation theory.

5. The evolution lines of Wannier centers for tetradymite $BiSbTe_3$

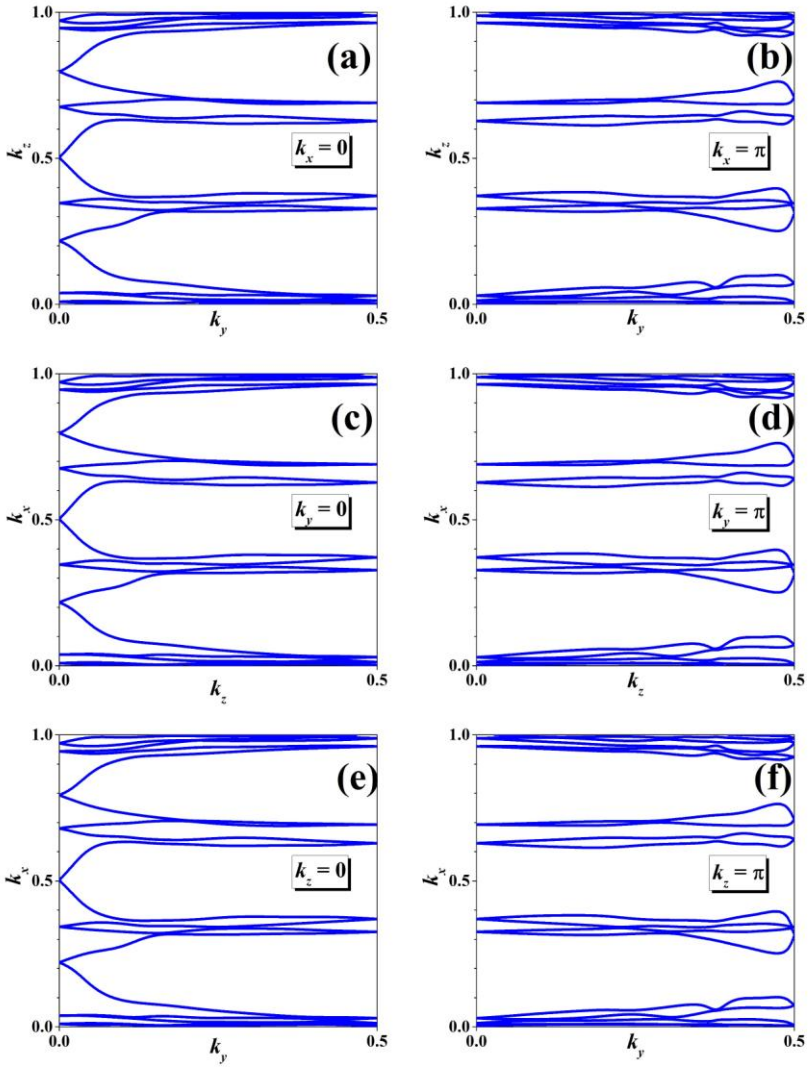

Figure S5. (a)~(f) Calculated evolution lines of Wannier centers in $\boldsymbol{k_x} = 0$, $\boldsymbol{k_x} = \pi$, $\boldsymbol{k_y} = 0$, $\boldsymbol{k_y} = \pi$, $\boldsymbol{k_z} = 0$, and $\boldsymbol{k_z} = \pi$ planes.

6. The graphical representation of the distribution of the symmetry protected Weyl points

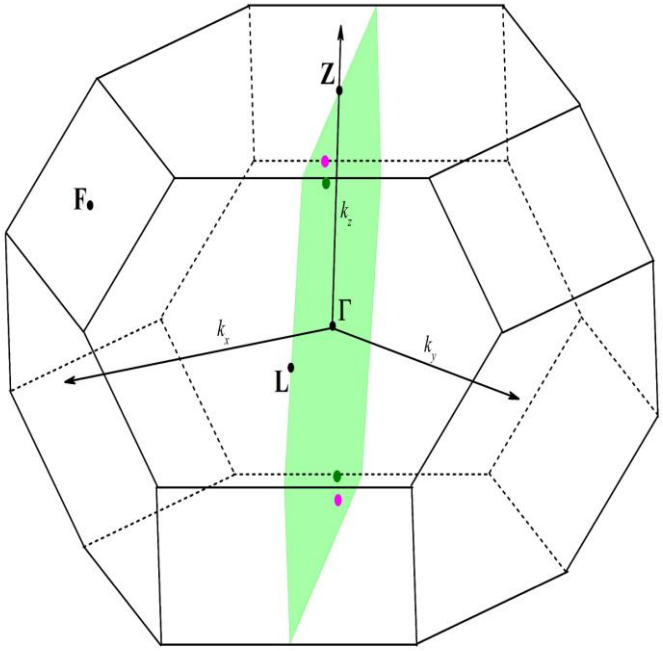

Figure S6. The graphical representation of the distribution of the symmetry protected Weyl points and the high-symmetry $k_x = k_y$ plane (highlighted in green).

The real-lattice ($\boldsymbol{a}_1$, $\boldsymbol{a}_2$, $\boldsymbol{a}_3$ for primitive cell and $\boldsymbol{b}_1$, $\boldsymbol{b}_2$, $\boldsymbol{b}_3$ for conventional cell, as marked in Fig. 1) can be expressed as

$$\begin{gathered}\boldsymbol{a}_1 = -\frac{a}{2}\hat{i} - \frac{\sqrt{3}}{6}a\hat{j} + \frac{c}{3}\hat{k},\ \boldsymbol{a}_2 = \frac{a}{2}\hat{i} - \frac{\sqrt{3}}{6}a\hat{j} + \frac{c}{3}\hat{k},\ \boldsymbol{a}_3 = \frac{\sqrt{3}}{3}a\hat{j} + \frac{c}{3}\hat{k}, \\ \boldsymbol{b}_1 = -\frac{a}{2}\hat{i} + \frac{\sqrt{3}}{2}a\hat{j},\ \boldsymbol{b}_2 = a\hat{i},\ \boldsymbol{b}_3 = c\hat{k}\end{gathered}, \quad (1)$$

The reciprocal-lattice vectors $\boldsymbol{t}_{1,2,3}$ are defined by $\boldsymbol{t}_i \cdot \boldsymbol{a}_j = 2\pi\delta_{ij}$, are given as

$$\boldsymbol{t}_1 = \frac{2\pi}{a}\left(-\hat{i} - \frac{\sqrt{3}}{3}\hat{j} + \frac{a}{c}\hat{k}\right),\ \boldsymbol{t}_2 = \frac{2\pi}{a}\left(\hat{i} - \frac{\sqrt{3}}{3}\hat{j} + \frac{a}{c}\hat{k}\right),\ \boldsymbol{t}_3 = \frac{2\pi}{a}\left(\frac{2\sqrt{3}}{3}\hat{j} + \frac{a}{c}\hat{k}\right), \quad (2)$$

Here $\hat{i}$, $\hat{j}$, and $\hat{k}$ represent the unit vector of k_x, k_y, and k_z in Cartesian coordanates, respectively. a and c are the optimized lattice parameters of conventional cell.

7. The Fermi surface map and the spin texture in the (001) plane

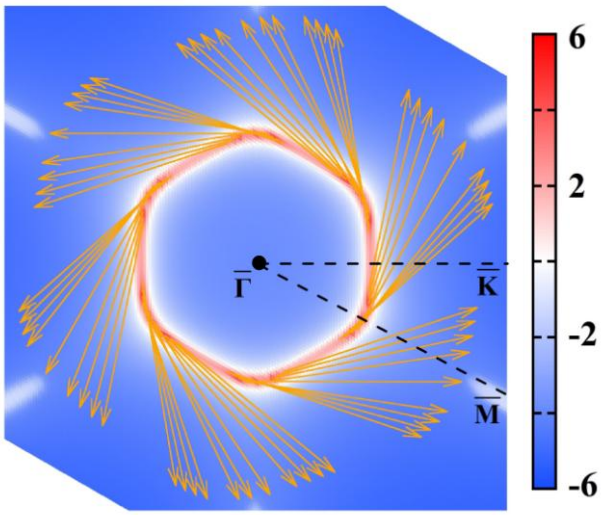

Figure S7. The Fermi surface mapped in the (001) plane as well as the spin texture at the energy of −0.1 eV.

8. Bands structures projected onto $k_x = k_y$ surface

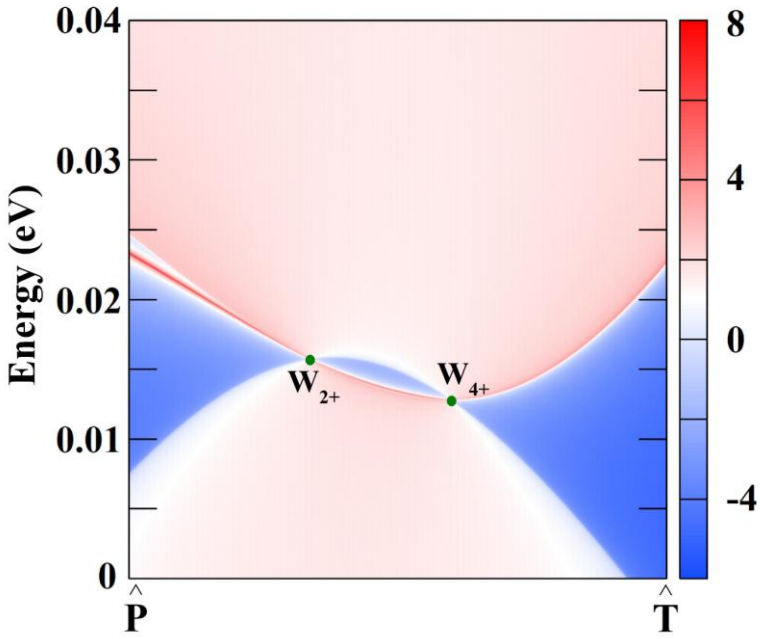

Figure S8. The $k_x = k_y$ plane surface state of $BiSbTe_3$ in $\hat{\mathbf{P}}-\hat{\mathbf{T}}$ line (Perpendicular to $\hat{\Gamma}$-$\hat{\mathbf{R}}$ direction).

9. The coordinates of Weyl points under out-of-plane strains

Table R1. The coordinates in momentum space and the chirality of Weyl points in $k_x = k_y$ plane with 2% compressive and tensile strains along interlayer directions.

		Coordinate	Chirality
$c = 0.98\ c_0$	W_{1-}	(−0.411, −0.411, −0.324)	−1
	W_{1+}	(−0.394, −0.394, −0.307)	+1
	W_{3-}	(0.411, 0.411, 0.324)	−1
	W_{3+}	(0.394, 0.394, 0.307)	+1
$c = 1.02\ c_0$	W_{1-}	(−0.432, −0.432, −0.330)	−1
	W_{1+}	(−0.412, −0.412, −0.310)	+1
	W_{3-}	(0.432, 0.432, 0.330)	−1
	W_{3+}	(0.412, 0.412, 0.310)	+1

10. The evolution lines of Wannier centers for $BiSbTe_3$ with strains

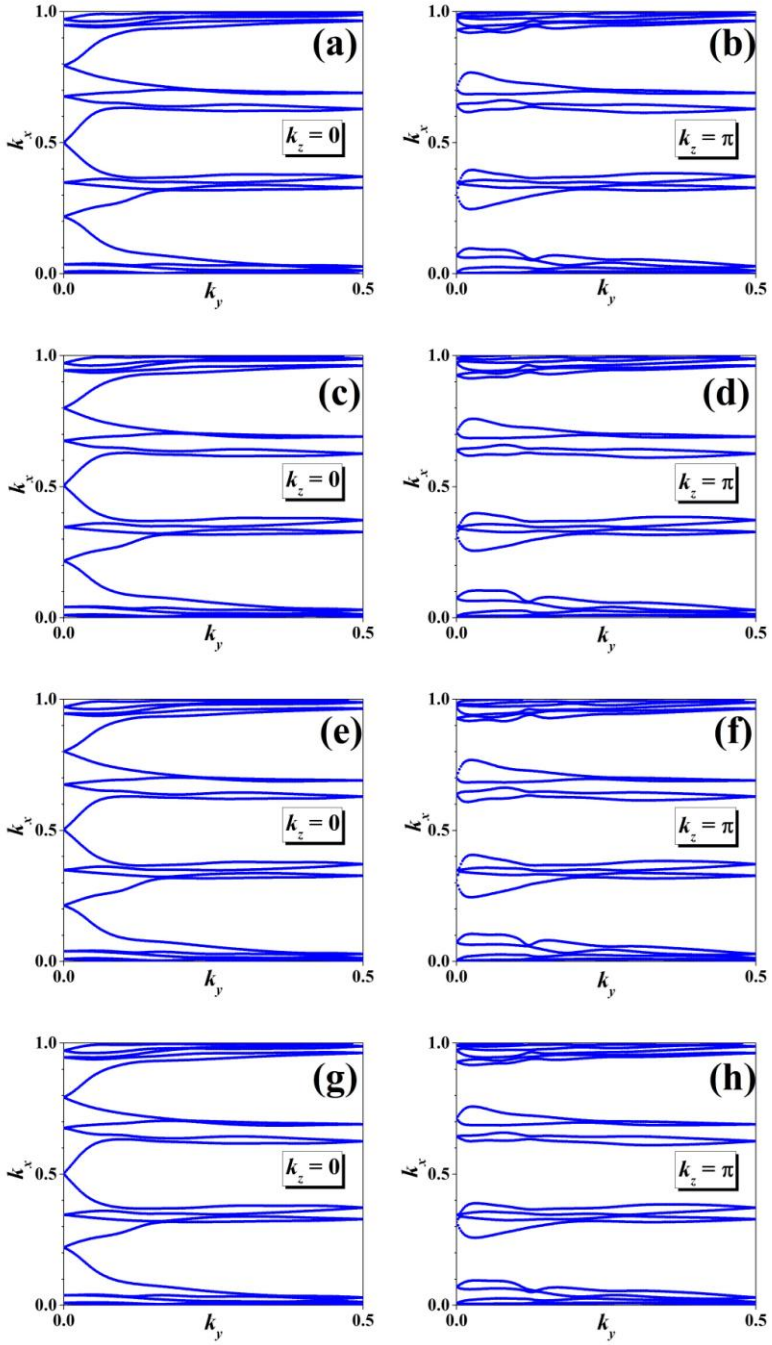

Figure S9. Calculated evolution lines of Wannier centers in $\boldsymbol{k_z} = 0$ and $\boldsymbol{k_z} = \pi$ planes under (a)~(b) 2% in-plane compressive strains, (c)~(b) 2% in-plane tensile strains, (e)~(f) 2% out-of-plane compressive strains, and (g)~(h) 2% out-of-plane tensile strains.